Solidification Characteristics and Eutectic Precipitates in 15Cr–22Ni–1Nb Austenitic Heat-Resistant Stainless Steel

XIN ZHU, CHENGBIN SHI, HUAI ZHANG, JING LI, and JUN LIU

The influence of the cooling rate of liquid steel on solidification characteristics, eutectic NbC and Laves phase in 15Cr–22Ni–1Nb steel was investigated *via in situ* observation and microstructure characterization. The initiation and finishing solidification temperatures of the steel increase first and then decrease as the cooling rate is increased from 10 to 100 °C/min, whereas its solidification temperature interval is monotonically enlarged. The rate constant of austenitic nucleation and growth decreases with the increase in cooling rate because of the reduction in the effective activation energy of liquid steel solidification. The nucleation rate of austenite continuously increases with increasing the cooling rate. The effective activation energy of austenitic nucleation and growth is -88.86 and -396.76 kJ/mol, respectively. The secondary dendrite arm spacing of the steel is reduced from 69.43 to 27.27 μm as the cooling rate is increased from 10 to 100 °C/min. Increasing the cooling rate aggravates the microsegregation degree of C, Si, Ni, Cr, Nb and Mo, which enhances the generation of eutectic NbC and Laves phase. The volume fractions and number densities of eutectic NbC and Laves phase increase with increasing the cooling rate. The mass ratio of Nb/C in the residual liquid steel increases as the cooling rate is increased, which is favorable to the precipitation of Laves phase. The starting-precipitation solid fraction and starting-precipitation temperature of eutectic NbC and Laves phase increase initially and then decrease with increasing the cooling rate. The precipitation tendency of eutectic NbC and Laves phase is enhanced as the cooling rate is increased.

I. INTRODUCTION

15CR–22NI–1NB austenitic heat-resistant stainless steel is developed for vital components and parts serving at moderately elevated temperature in the petrochemistry, aerospace and steam generation industries, such as heat exchangers, turbine disks, rotor blades, and main steam tubes.[1–3] Since 15Cr–22Ni–1Nb steel possesses high concentrations of alloying elements (approximately 41 mass pct), large eutectic precipitates are inevitably generated during liquid steel solidification.[1,2] These large eutectic precipitates in the steel could hardly be eliminated in the subsequent deformation and heat treatment, especially large eutectic NbC.[3–5] Stress concentration often occurs around these large eutectic precipitates, which easily causes the initiation and propagation of microcracks and weakens the mechanical properties of steel.[6–9] It is quite important to investigate the solidification characteristics of 15Cr–22Ni–1Nb steel and inhibit the generation of large eutectic precipitates.

The cooling rate of liquid steel exerts a great influence on the solidification characteristics and eutectic precipitates in steel. Bleckmann *et al.*[10] found that the initiation and finishing solidification temperatures of Fe–4.2Cr–2.1V–1C steel were lowered with increasing the cooling rate, whereas the solidification temperature interval was enlarged. Wang *et al.*[11] reported that the nucleation density and growth velocity of austenite grains in high-molybdenum austenite stainless steel increased as the cooling rate was increased, resulting in a finer as-cast structure. Zhou *et al.*[12] found that the morphology of M_2C carbides in AISI M2 high speed steel changed from plate-like to fibrous type with increasing the cooling rate. Liu *et al.*[13] showed that the quantity and volume of eutectic carbides in D2 cold work die steel increased with the increase in cooling rate, but the carbides gradually grew finer from slats to

XIN ZHU, CHENGBIN SHI, HUAI ZHANG, JING LI, and JUN LIU are with the State Key Laboratory of Advanced Metallurgy, University of Science and Technology Beijing (USTB), Beijing 100083, China. Contact e-mail: chengbin.shi@ustb.edu.cn

fibrous morphology. Hao et al.[14] reported that the microsegregation degree of molybdenum, chromium and nickel in 20.5Cr–24.5Ni–6Mo super austenitic stainless steel were reduced as the cooling rate was increased, and thus the volume fraction of eutectic precipitates was lowered. It is of great importance to study the influence of cooling rate on solidification characteristics and eutectic precipitates to improve the high temperature mechanical properties of 15Cr–22Ni–1Nb steel.

In the present study, the effect of cooling rate on solidification characteristics of 15Cr–22Ni–1Nb steel was investigated by in situ observation experiments and Johnson–Mehl–Avrami–Kologoromov (JMAK) model. The morphological dimension, volume fraction and number density of eutectic NbC and Laves phase were studied. Meanwhile, the change in the atomic percentage of Laves phase-forming alloying element with cooling rate was illustrated. Furthermore, the relationship between microsegregation degree of alloying elements and cooling rate was analyzed using various microsegregation models. Thermodynamic considerations were conducted to study the formation of eutectic NbC and Laves phase.

II. EXPERIMENTAL PROCEDURE

A. Materials Preparation

15Cr–22Ni–1Nb steel was produced by vacuum induction melting (VIM), followed by protective argon gas atmosphere electroslag remelting (ESR). The chemical composition of the remelted ingot is shown in Table I. Specimens (ϕ 7.5 mm × 3.5 mm) were cut from the as-cast remelted ingot, and then mechanically polished and ultrasonically cleaned for in situ observation experiments.

B. In Situ Observation of Liquid Steel Solidification Using CLSM

In order to reveal the solidification characteristics of 15Cr–22Ni–1Nb steel at different cooling rates, in situ observation of liquid steel solidification was conducted using confocal laser scanning microscopy (CLSM, VL2000DX-SVF17SP, LASERTEC Inc., Japan). The prepared specimen was placed in a high-purity alumina crucible (ϕ 8 mm × 4 mm), and then the crucible was inserted into the reaction chamber of CLSM. The chamber was vacuumized three times and then filled with high-purity argon to avoid the oxidation of the sample. The specimen was heated from room

temperature to 1723 K (1450 °C) at the rate of 200 °C/min, and then kept isothermally for 5 min to ensure the complete melting of the specimen and the uniformity of liquid steel composition. Subsequently, the liquid specimen was cooled to room temperature at the rates of 10, 25, 50 and 100 °C/min in individual experiment, respectively.

C. Microstructure Characterization

The specimens after in situ observation experiments were mounted, polished, and etched with a solution of 5 g $CuCl_2$ + 30 mL HCl + 30 mL H_2O + 25 mL anhydrous alcohol. The as-cast microstructure of the etched specimens was observed using an optical microscope (OM, DM4 M, Leica, Germany). The secondary dendrite arm spacing in ten randomly selected OM images was measured by Image-Pro Plus software. The polished specimens were electrolytically etched with a solution of 1 g tetramethylammonium chloride + 10 mL acetylacetone + 89 mL anhydrous alcohol at a voltage of 20-volt for 4 min. The three-dimensional morphologies of eutectic NbC and Laves phase were observed using a scanning electron microscope (SEM, FEI Quanta-250, FEI Corporation, Hillsboro, OR) equipped with an energy-dispersive X-ray spectrometer (EDS, XFlash 5030, Bruker, Germany). In addition, twenty-five SEM images magnified 1500 times were randomly selected to count the volume fraction and number density of eutectic NbC and Laves phase. Twenty-five EDS point analyses of Laves phase were randomly chose to determine the atomic percentages of Laves phase-forming alloying elements.

III. RESULTS AND DISCUSSION

A. Solidification Characteristics of 15Cr–22Ni–1Nb Steel

1. In situ observation of liquid steel solidification
Figure 1 illustrates the solidification process of 15Cr–22Ni–1Nb steel during continuous cooling at 10 °C/min. As presented in Figure 1(a), the point-like prior austenite first observed on the liquid steel surface is regarded as the initial nucleation site, corresponding to the initiation of austenite formation (initiation solidification temperature 1666.7 K (1393.7 °C)). It can be seen from Figure 1(b) through (f) that the austenite phase constantly grows and the residual liquid phase continues to shrink until the liquid steel is completely solidified (finishing solidification temperature 1638.1 K (1365.1 °C)). The solidification temperature interval and final solidification time of the steel during continuous cooling at 10 °C/min are 28.6 K (28.6 °C) and 157 seconds, respectively.

Figure 2 presents the CSLM images of liquid steel solidification at different cooling rates when the time was increased by 16 s from initial nucleation. A higher cooling rate promotes a greater solid fraction. Meanwhile, as shown in Figure 2, the temperature of liquid steel was increased from 1662.8 K to 1672.8 K

Table I. Chemical Composition of 15Cr–22Ni–1Nb Steel (Mass Pct)

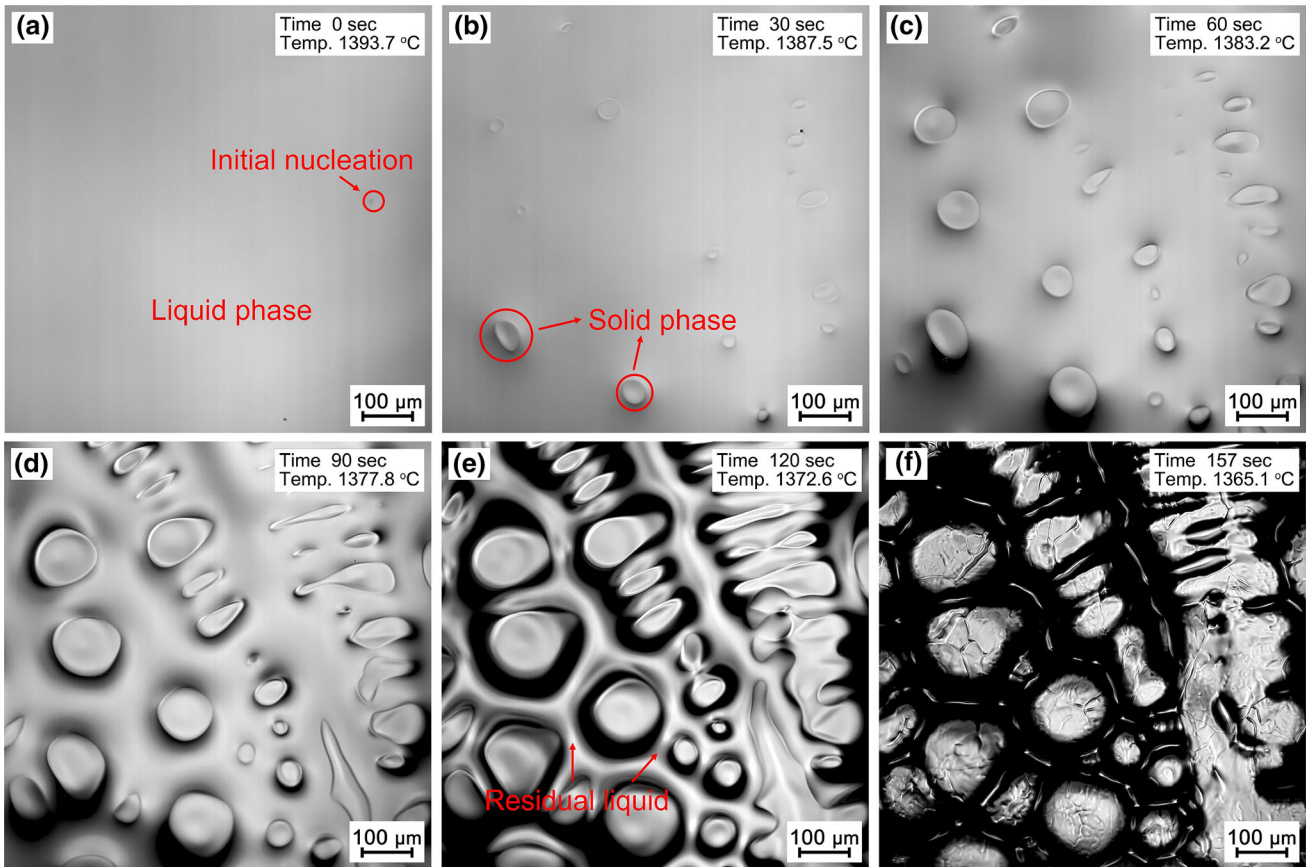| C	Si	Mn	Ni	Cr	Mo	Nb	Al	Ti
0.02	0.50	0.82	22	15.5	2.6	1.0	0.19	0.13

Fig. 1—CSLM images of liquid steel solidification at the cooling rate of 10 °C/min. (*a*) 0 s, (*b*) 30 s, (*c*) 60 s, (*d*) 90 s, (*e*) 120 s, (*f*) 157 s.

(1389.8 °C to 1399.8 °C) with increasing the cooling rate from 10 to 25 °C/min, whereas it decreases from 1672.8 K to 1610.7 K (1399.8 °C to 1337.7 °C) when the cooling rate increases from 25 to 100 °C/min. This is because the initiation solidification temperature of the steel increases as the cooling rate is increased from 10 to 25 °C/min, and decreases as the cooling rate is increased from 25 to 100 °C/min. When the temperature of liquid steel was decreased by 16 K (16 °C) from initial nucleation, the CSLM images of liquid steel solidification at different cooling rates is shown in Figure 3. It can be learned that a higher cooling rate has a smaller solid fraction when the decrease in the temperature is consistent, indicating that a higher cooling rate results in a larger solidification temperature interval.

Figure 4 shows the change in the initiation solidification temperature (T_{INI}), finishing solidification temperature (T_{FIN}) and solidification temperature interval ($T_{INR} = T_{INI} - T_{FIN}$) of 15Cr–22Ni–1Nb steel with cooling rate. As the cooling rate is increased from 10 to 25 °C/min, the initiation solidification temperature of the steel increases from 1666.7 K to 1681.6 K (1393.7 °C to 1408.6 °C) and the finishing solidification temperature increases from 1638.1 K to 1648.9 K (1365.1 °C to 1375.9 °C). However, the initiation solidification temperature decreases from 1681.6 K to 1642.7 K (1408.6 °C to 1369.7 °C) and the finishing solidification temperature decreases from 1648.9 K to 1592.5 K (1375.9 °C to

1319.5 °C) when the cooling rate is increased from 25 to 100°C/min. Furthermore, it can be learned from Figure 4 that the solidification temperature interval of the steel increases from 28.6 K to 50.2 K (28.6 °C to 50.2 °C) with increasing the cooling rate from 10 to 100 °C/min.

Figure 5 shows the change in the final solidification time (the time at which liquid steel is fully solidified) of 15Cr–22Ni–1Nb steel with cooling rate. The final solidification time of the steel is 157, 71, 42 and 25 s at the cooling rates of 10, 25, 50 and 100 °C/min, respectively. In addition, the relationship between final solidification time and cooling rate of liquid steel is established as Eq. [1]. The correlation coefficient R^2 is 0.999.

$$t_f = 35.04 \cdot v^{-0.83} \qquad [1]$$

where t_f is the final solidification time (s), v is the cooling rate of liquid steel (°C/s).

2. *Nucleation and growth of austenite*

The nucleation and growth of austenite directly determines the solidification microstructure of 15Cr–22Ni–1Nb steel. Hence, it is of great importance to investigate the characteristics of austenitic nucleation and growth during the solidification of 15Cr–22Ni–1Nb steel. The Johnson–Mehl–Avrami–Kologoromov (JMAK) model is employed to describe the overall kinetics of isothermal phase transformation *via*
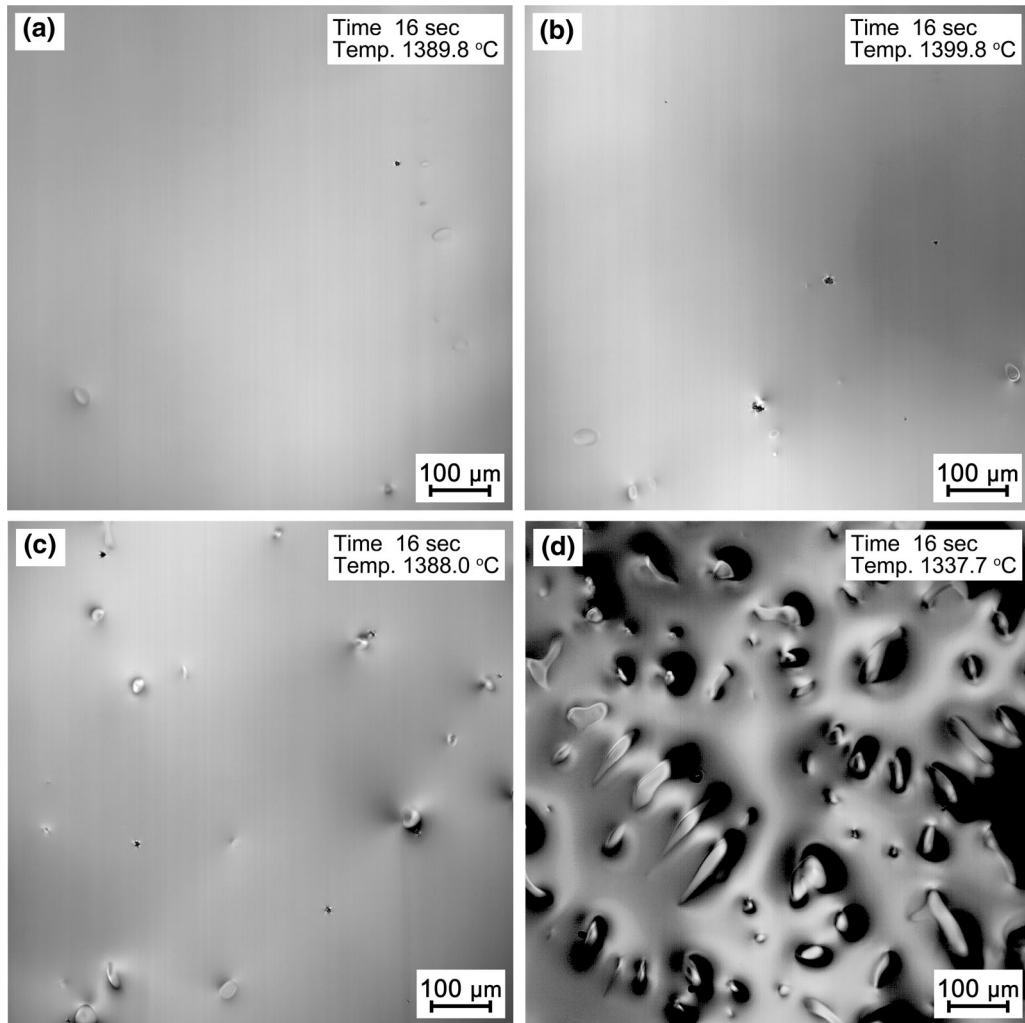
Fig. 2—CSLM images of liquid steel solidification at different cooling rates when the time was increased by 16 s from initial nucleation. (a) 10 °C/min, (b) 25 °C/min, (c) 50 °C/min, (d) 100 °C/min.

nucleation and growth.[15] Some researchers point out that the JMAK model can also be used to the non-isothermal solidification in the case where the nucleation occurs in the early stage of solidification and becomes negligible afterward.[16–18] Several researchers used the modified JMAK model to the non-isothermal phase transformation because most of thermal histories in real applications are continuous cooling paths.[19–21]

In the current study, the austenitic nucleation and growth in the early stage of solidification is described with the JMAK model, as expressed in Eq. [2].[15]

$$x = 1 - \exp(-kt^n) \qquad [2]$$

Meanwhile, taking twice the natural logarithm of Eq. [2] gives the following expression:

$$\ln[-\ln(1-x)] = n \ln t + \ln k \qquad [3]$$

where x is the solid fraction, t is the solidification time (s), n is the Avrami exponent, which is used to characterize the nucleation mechanism during phase transformation.[22,23] The value of $n < 3$ indicates that the

nucleation mechanism is site saturation nucleation and the nucleation process only occurs at the initial stage of phase transformation. The range of $3 < n < 4$ indicates that there is still a decreasing nucleation rate after site saturation nucleation. The value of $n > 4$ corresponds to site saturation nucleation plus an increasing nucleation rate. The rate constant k of nucleation and growth is given by Arrhenius equation,[15] as shown in Eq. [4].

$$k = k_0 \exp\left(-\frac{Q}{R\Delta T}\right) \qquad [4]$$

$$\Delta T = T - T_{\text{FIN}} \qquad [5]$$

where k_0 is the pre-exponent coefficient, Q is the effective activation energy of liquid steel solidification (J/mol), R is the gas constant of 8.314 J/(mol K), ΔT is the difference between real-time temperature T and finishing solidification temperature T_{FIN}.
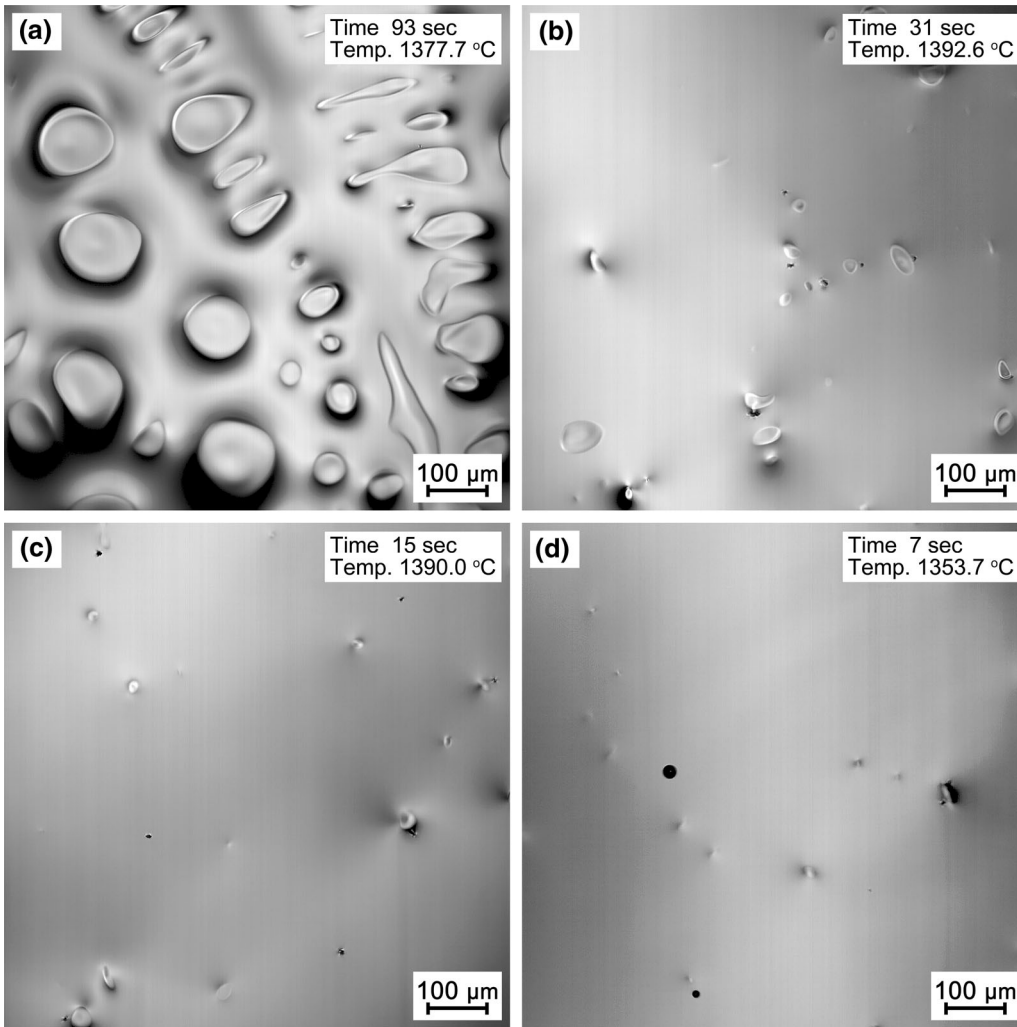
Fig. 3—CSLM images of liquid steel solidification at different cooling rates when the temperature was decreased by 16 K (16 °C) from initial nucleation. (*a*) 10 °C/min, (*b*) 25 °C/min, (*c*) 50 °C/min, (*d*) 100 °C/min.
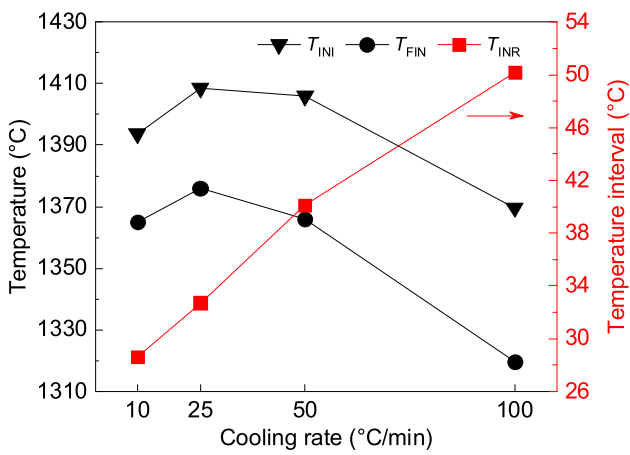

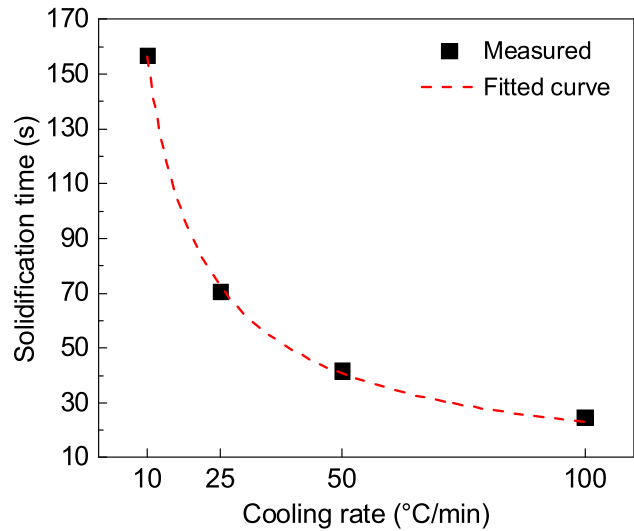Fig. 4—Change in the T_{INI}, T_{FIN} and T_{INR} of 15Cr–22Ni–1Nb steel with cooling rate.

Fig. 5—Relationship between the final solidification time and the cooling rate.
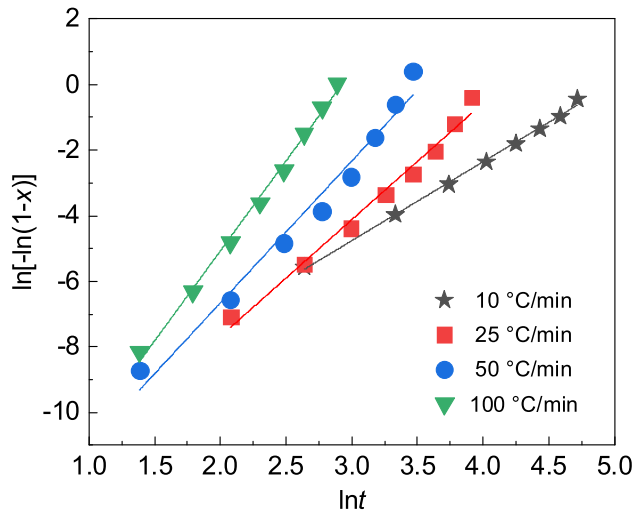
Fig. 6—Plots of ln[− ln(1−x)] *vs* ln*t* at different cooling rates.

Fig. 7—Plots of ln(− ln(x)) *vs* ln(ΔT) at different cooling rates.

Table II. Values of the Parameters *k* and *n*

Cooling Rate (°C/min)	k	n	R^2
10	6.21×10^{-6}	2.41	0.997
25	3.77×10^{-7}	3.56	0.984
50	2.29×10^{-7}	4.32	0.976
100	1.08×10^{-7}	5.48	0.995

Figure 6 presents the plots of ln[− ln(1−x)] *vs* ln*t* at the cooling rates of 10, 25, 50 and 100 °C/min. The calculated values of rate constant *k* and Avrami exponent *n* are given in Table II. The rate constant *k* of nucleation and growth decreases from 6.21×10^{-6} to 1.08×10^{-7} as the cooling rate is increased from 10 to 100 °C/min. It indicates that the effective driving force of austenitic nucleation and growth at the early period of solidification is smaller at a higher cooling rate, which tends to cause initial nucleation to occur at lower temperatures. It is noteworthy that the rate constant is greatly reduced with increasing the cooling rate from 10 to 25 °C/min, which could be due to the change in nucleation mechanism. As shown in Table II, the Avrami exponent *n* is calculated to be 2.41 and 3.56 at the cooling rate of 10 and 25 °C/min, respectively. It suggests that the nucleation changes from site saturation nucleation to site saturation nucleation plus a decreasing nucleation rate as the cooling rate is increased from 10 to 25 °C/min. Furthermore, the nucleation mechanism converts into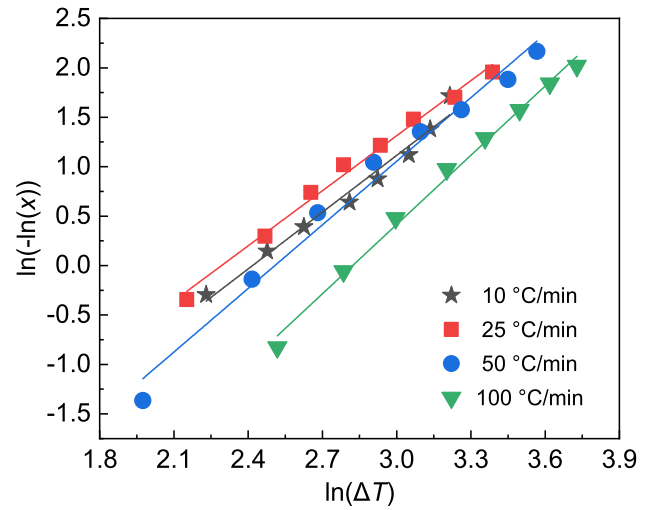 site saturation nucleation plus an increasing nucleation rate when the cooling rate is 50 and 100 °C/min. A higher cooling rate results in a greater nucleation rate of austenite, and thus initial nucleation is more likely to take place at higher temperatures.

To further clarify the role of cooling rate on the growth and nucleation of austenite during liquid steel solidification, the effective activation energy of liquid steel solidification is calculated by combining the JMAK model with Eq. [6].

$$x = \exp\left(-A\Delta T^B\right) \qquad [6]$$

The change in solid fraction with temperature difference is expressed as Eq. [6]. *A* and *B* in Eq. [6] is the coefficient.[22]

Taking twice the natural logarithm of Eq. [6] gives the Eq. [7].

$$\ln(-\ln(x)) = B\ln(\Delta T) + \ln A \qquad [7]$$

Figure 7 shows the plots of ln(− ln(x)) *vs* ln(ΔT) at different cooling rates. The parameters ln*A* and *B* can be determined from the intercept and slope of the fitted straight line, respectively. The values of the parameters *A* and *B* are listed in Table III. The parameters *A* and *B* are used to calculate the effective activation energy of liquid steel solidification.

Taking the derivative with respect to *t* on both sides of Eqs. [2] gives [8].

$$\frac{dx}{dt} = k^{1/n} \cdot F(x) \qquad [8]$$

F(x) in Eq. [8] can be expressed as Eq. [9].

Table III. Values of the Parameters A and B

Cooling Rate (°C/min)	A	B	R^2
10	9.75×10^{-3}	1.91	0.977
25	1.41×10^{-2}	1.86	0.992
50	4.61×10^{-3}	2.14	0.984
100	1.37×10^{-3}	2.33	0.994

Table IV. Values of the Parameters k_0 and Q

Cooling Rate (°C/min)	k_0	Q (kJ/mol)	R^2
10	2.15×10^{-7}	− 456.04	0.986
25	2.30×10^{-8}	− 385.36	0.993
50	2.52×10^{-8}	− 306.01	0.976
100	2.70×10^{-8}	− 233.73	0.987
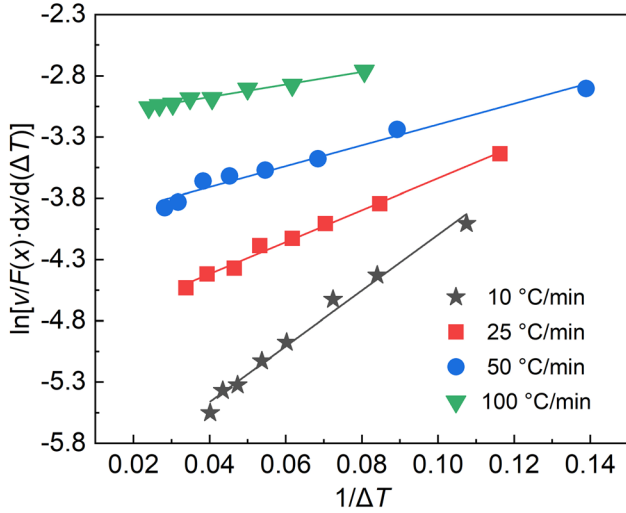
Fig. 8—Plots of $\ln[v/F(x)\cdot dx/d(\Delta T)]$ vs $1/\Delta T$ at different cooling rates.

Fig. 9—Plots of Q vs $1/n$.

$$F(x) = n \cdot (1 - x) \cdot (-\ln(1 - x))^{(n-1)/n} \qquad [9]$$

dx/dt can be written as the product of cooling rate v and $dx/d(\Delta T)$, as presented in Eq. [10].

$$\frac{dx}{dt} = \frac{dx}{d(\Delta T)} \cdot \frac{d(\Delta T)}{dt} = v \frac{dx}{d(\Delta T)} \qquad [10]$$

$dx/d(\Delta T)$ can be obtained by taking the derivative with respect to ΔT on both sides of Eq. [6], as shown in Eq. [11].

$$\frac{dx}{d(\Delta T)} = \exp(-A\Delta T^B) \cdot (-AB) \cdot \Delta T^{B-1} \qquad [11]$$

Inserting Eqs. [10] into [8], the following equation can be obtained.

$$\ln k = n \ln\left[\frac{v}{F(x)} \cdot \frac{dx}{d(\Delta T)}\right] \qquad [12]$$

Furthermore, $\ln k$ can be obtained by taking the natural logarithm on Eq. [4], as expressed by the following equation.

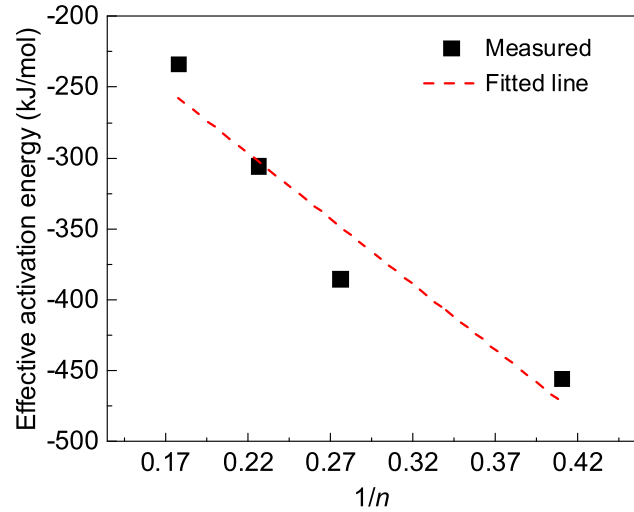$$\ln k = -\frac{Q}{R}(1/\Delta T) + \ln k_0 \qquad [13]$$

Taking Eqs. [13] into [12], Eq. [14] is obtained.

$$\ln\left[\frac{v}{F(x)} \cdot \frac{dx}{d(\Delta T)}\right] = -\frac{Q}{nR}(1/\Delta T) + \frac{\ln k_0}{n} \qquad [14]$$

Potting $\ln[v/F(x)\cdot dx/d(\Delta T)]$ vs $1/\Delta T$ gives the slope $(-Q/nR)$ and intercept $(\ln k_0/n)$ of Eq. [14]. The effective activation energy Q of liquid steel solidification can be obtained by taking the Avrami exponent n and the gas constant R into $-Q/nR$.

Figure 8 shows the plots of $\ln[v/F(x)\cdot dx/d(\Delta T)]$ vs $1/\Delta T$ at the cooling rates of 10, 25, 50 and 100 °C/min. The values of the parameters k_0 and Q are given in Table IV. The effective activation energy Q of liquid steel solidification is − 456.04, − 385.36, − 306.01 and − 233.73 kJ/mol at the cooling rates of 10, 25, 50 and 100 °C/min, respectively. Hence, a lower cooling rate gives a greater effective driving force for nucleation and growth in the initial stage of nucleation and growth. This is the reason why the lower cooling rate instead leads to a larger rate constant of austenitic nucleation and growth. Furthermore, the role of cooling rate on austenitic growth and nucleation is investigated by calculating the effective activation energy of austenitic nucleation and growth.

The effective activation energy Q can be interpreted as a weighted sum of nucleation activation energy Q_N and growth activation energy Q_G with $(1-d/nm)$ and (d/nm) as the weighing factors, as shown in Eq. [15].[24]

$$Q = (1 - d/nm)Q_N + (d/nm)Q_G \qquad [15]$$

where d is the growth dimensionality ($d = 3$), and m is the growth mode parameter ($m = 1$ for interface-controlled growth in the current study). Therefore, Eq. [15] can be further rewritten as Eq. [16] for the linear fitting.

$$Q = (3Q_G - 3Q_N) \cdot \left(\frac{1}{n}\right) + Q_N \qquad [16]$$

The linear fitting is conducted between Q and $1/n$ according to Eq. [16], as shown in Figure 9. The nucleation activation energy Q_N and growth activation energy Q_G are -88.86 and -396.76 kJ/mol, respectively. The correlation coefficient R^2 is 0.921. The austenitic nucleation and growth during liquid steel solidification tends to the direction of significant drop of energy. Since the nucleation activation energy during the solidification of 15Cr–22Ni–1Nb steel is markedly lower than the growth activation energy, a higher cooling rate promotes a greater nucleation rate. At a higher cooling rate, a larger number of micro-scale nucleation is in a metastable state at the initial stage of solidification, which is easier to appear on the macro scale in the unstable solidification process.[25] Therefore, initial nucleation is more likely to occur at higher temperatures in the unstable solidification process when the cooling rate is higher.

3. As-cast microstructure of 15Cr–22Ni–1Nb steel

The as-cast microstructure of the specimens after *in situ* observation experiments is presented in Figure 10. It can be observed that the as-cast microstructure of the steel becomes finer with the increase in cooling rate. Meanwhile, the measured secondary dendrite arm spacing of
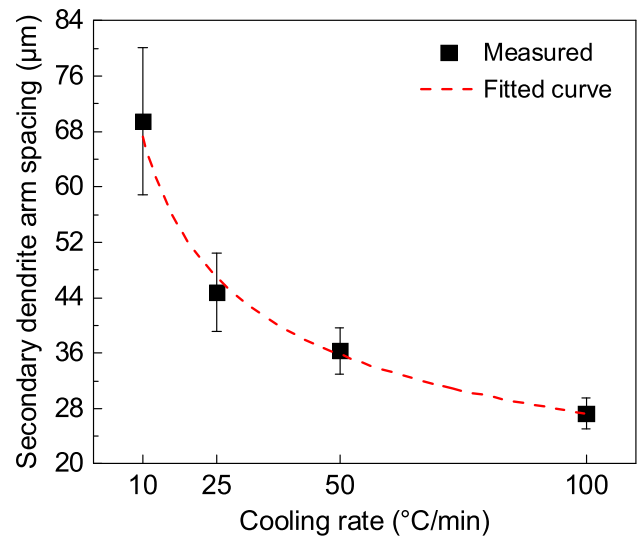
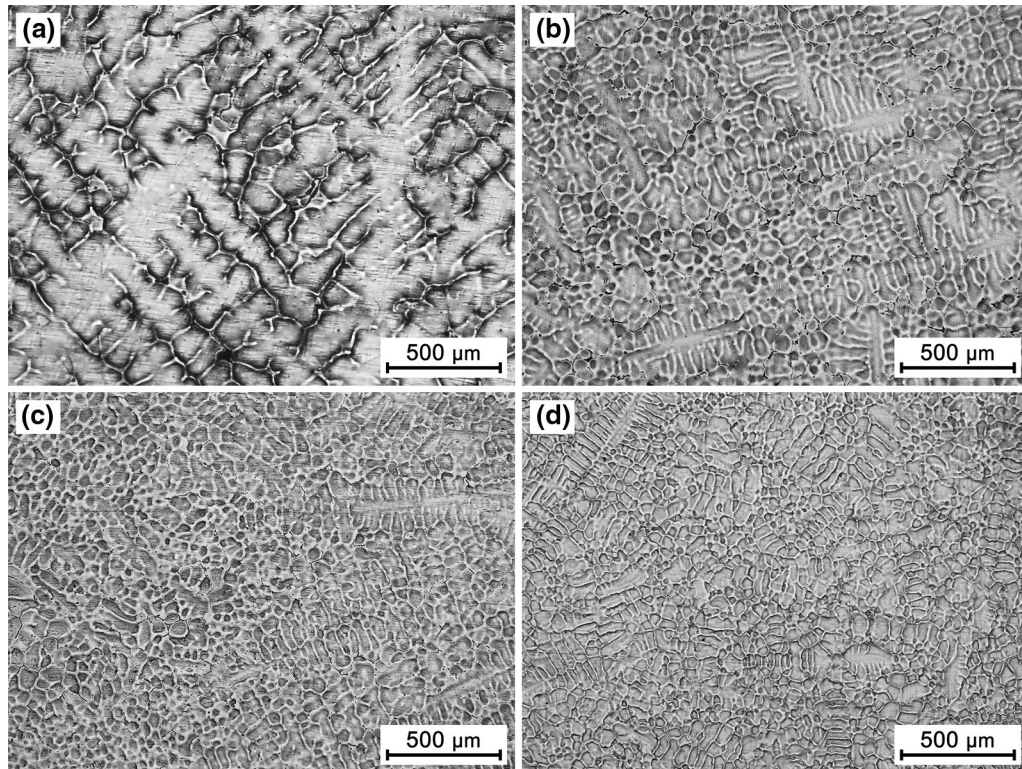Fig. 11—Change in the secondary dendrite arm spacing of 15Cr–22Ni–1Nb steel with cooling rate.

Fig. 10—As-cast microstructure of the specimens after *in situ* observation experiments. (*a*) 10 °C/min, (*b*) 25 °C/min, (*c*) 50 °C/min, (*d*) 100 °C/min.
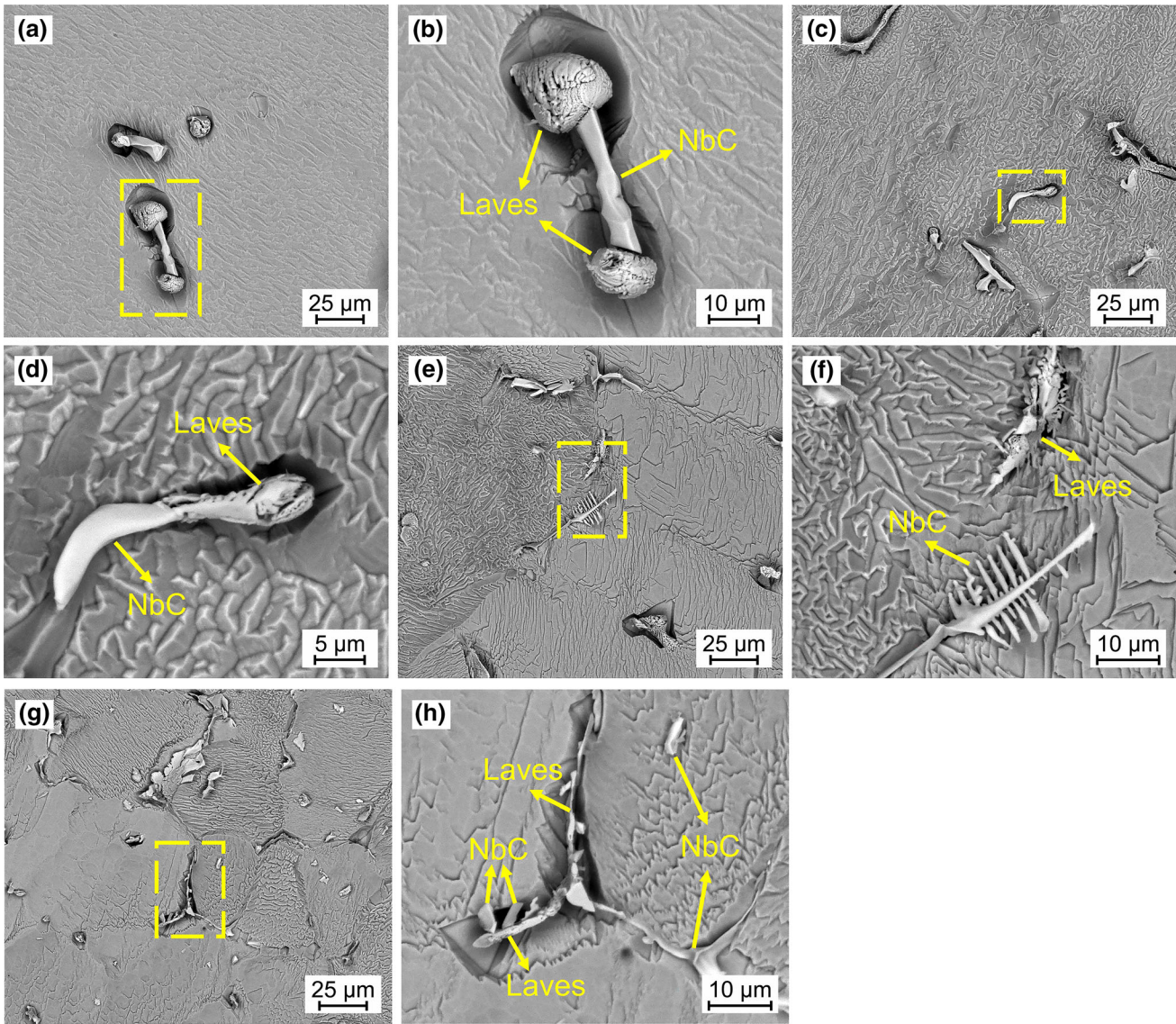
Fig. 12—Three-dimensional morphology of eutectic NbC and Laves phase at different cooling rates. (*a*) and (*b*) 10 °C/min, (*c*) and (*d*) 25 °C/min, (*e*) and (*f*) 50 °C/min, (*g*) and (*h*) 100 °C/min.

the steel is 69.43, 44.78, 36.35 and 27.27 μm at the cooling rates of 10, 25, 50 and 100 °C/min, respectively, as shown in Figure 11. The nucleation rate of austenite during liquid steel solidification is increased with the increase in cooling rate, resulting in a finer as-cast microstructure.

The crystal morphology and solidification microstructure of alloys are determined by the temperature gradient (G, °C/mm) and solidification growth rate (V, mm/min).[9] Many studies show that the secondary dendrite arm spacing varies as a function of temperature gradient and solidification growth rate, as expressed in Eq. [17].[9,14,26]

$$\lambda_2 = \beta \cdot (GV)^{-b} \qquad [17]$$

where λ_2 is the secondary dendrite arm spacing (μm), β and b is the material constant of an alloy, GV is the local cooling rate (°C/min). The function fitting is conducted for the secondary dendrite arm spacing and the local cooling rate according to Eq. [17], as presented in Figure 11. The fitted result shows that the material constant β is 165.56, b is 0.39. The correlation coefficient R^2 is 0.991. Therefore, the relationship between the secondary dendrite arm spacing and the local cooling rate for 15Cr–22Ni–1Nb steel can be described as Eq. [18].

$$\lambda_2 = 165.56 \cdot (GV)^{-0.39} \qquad [18]$$

According to Eq. [18], the local cooling rate at different positions of as-cast ingot can be obtained by measuring the corresponding secondary dendrite arm spacing, which is helpful to determine the solidification characteristics of 15Cr–22Ni–1Nb ingots with different scales.
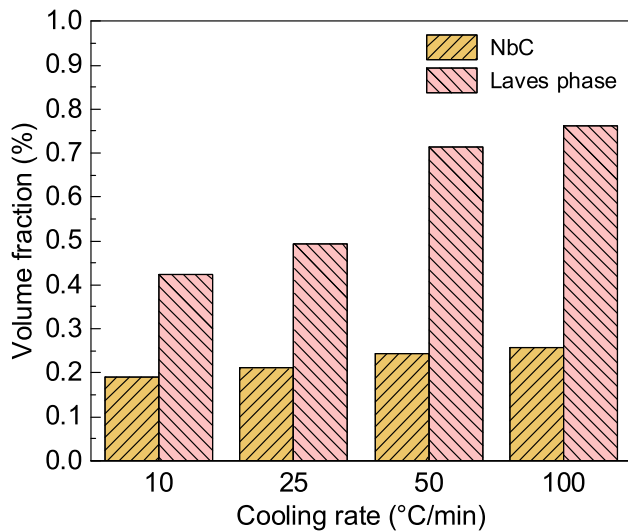
Fig. 13—Volume fraction of eutectic precipitates in 15Cr–22Ni–1Nb steel at different cooling rates.
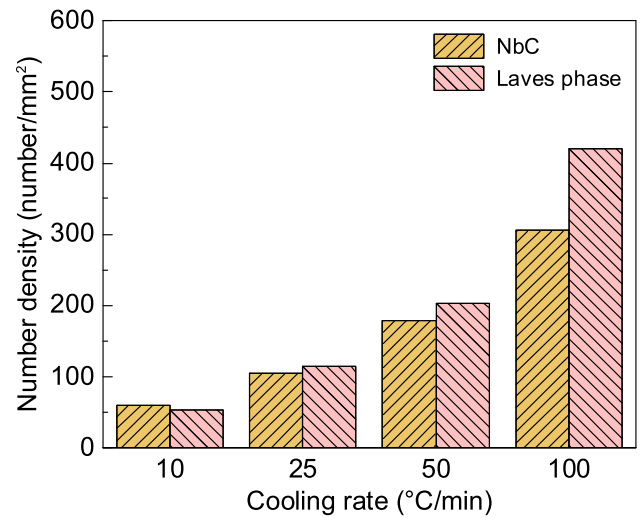

Fig. 14—Number density of eutectic precipitates in 15Cr–22Ni–1Nb steel at different cooling rates.

B. Eutectic Precipitates in 15Cr–22Ni–1Nb Steel

1. Characterization of eutectic precipitates

Figure 12 shows the three-dimensional morphology of eutectic precipitates in 15Cr–22Ni–1Nb steel at different cooling rates. It can be inferred from Figure 12(a), (c), (e) and (g) that the proportion of eutectic precipitates in the steel increases and their size decreases with the increase in cooling rate. As presented in Figures 12(a) through (d), the eutectic NbC appears blocky and Laves phase appears honeycomb in the steel at the cooling rate of 10 and 25 °C/min. Due to the reduction in the secondary dendrite arm spacing with increasing the cooling rate, the morphology of eutectic NbC and Laves phase precipitated at the terminal stage of solidification is continuously compressed, as shown in Figures 12(e) through (h).

The volume fraction of eutectic NbC and Laves phase in 15Cr–22Ni–1Nb steel at different cooling rates are presented in Figure 13. The volume fractions of Laves phase in the steel is greater than those of eutectic NbC at all cooling rates. This is because the mass ratio of Nb/C in the steel is greater than 40, and thus the Fe_2Nb-type Laves phase is mainly precipitated during liquid steel solidification.[1,4] The volume fraction of eutectic NbC in the steel increases from 0.19 to 0.26 pct, and that of Laves phase increases from 0.42 to 0.76 pct as the cooling rate of liquid steel is increased from 10 to 100 °C/min. It is noted that the influence of cooling rate on the volume fraction of Laves phase is more significant than that on NbC. Specifically, as the cooling rate is increased from 25 to 50 °C/min, the volume fraction of Laves phase increases from 0.49 to 0.71 pct, whereas that of NbC only increases from 0.21 to 0.24 pct. A further increase in cooling rate from 50 to 100 °C/min
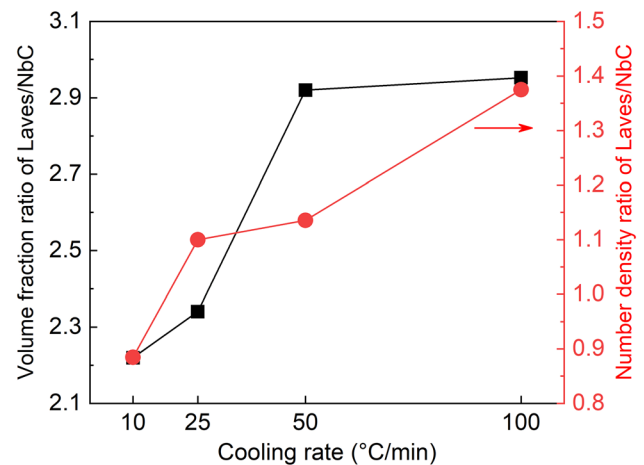

Fig. 15—Changes in the volume fraction ratio and number density ratio of Laves/NbC with cooling rate.

does not significantly enhance the volume fractions of eutectic NbC and Laves phase in the steel. It is because the extremely short time and the quite narrow space at the high cooling rate of 100 °C/min inhibits the formation of eutectic precipitates.

The volume fraction of eutectic NbC and Laves phase increases with the increase in cooling rate, indicating that the microsegregation degree of alloying elements is enhanced. In the process of liquid steel solidification, the back diffusion of alloying elements is the decisive factor to determine the microsegregation degree of alloying elements.[26] The reduction in the final solidification time with increasing the cooling rate restrains the back diffusion of alloying elements from liquid to solid phase. Consequently, more alloying elements is enriched in the
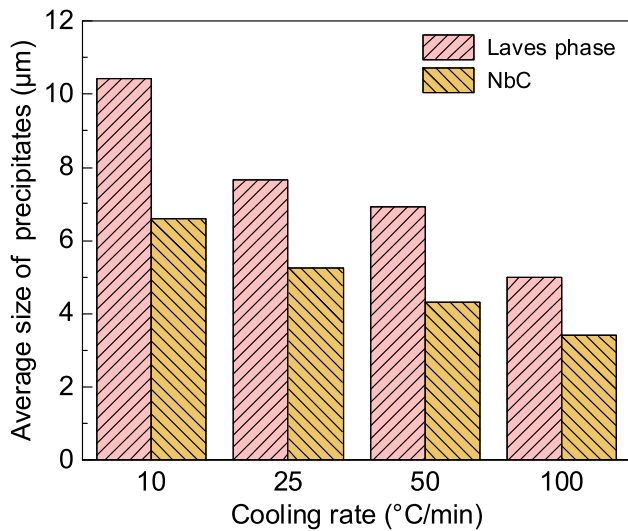
Fig. 16—Average size of eutectic precipitates in 15Cr–22Ni–1Nb steel at different cooling rates.

Fig. 17—Atomic percentage of Laves phase-forming alloying element in 15Cr–22Ni–1Nb steel at different cooling rates.

residual liquid phase at a higher cooling rate. Hence, the microsegregation degree of the alloying elements in the steel is enhanced as the cooling rates increases (a detailed discussion is presented in Section III–B–2).

The number density of eutectic NbC and Laves phase is increased with increasing the cooling rate, as presented in Figure 14. As the cooling rate is increased from 10, 25, 50 to 100 °C/min, the number density of eutectic NbC increases from 60.12, 104.05, 179.19 to 305.20 number/mm^2, and that of Laves phase increases from 53.18, 114.45, 203.47 to 419.65 number/mm^2. It indicates that the nucleation sites of NbC and Laves phase increase with the increase in cooling rate, which is due to the refinement of solidification structure. Furthermore, the number density of NbC particles in the steel is greater than that of Laves phase only at the cooling rate of 10 °C/min. It could be because the precipitation of eutectic NbC is prior to the Laves phase during the solidification of 15Cr–22Ni–1Nb steel.[1,2]

Figure 15 shows the changes in volume fraction ratio and number density ratio of Laves/NbC in 15Cr–22Ni–1Nb steel with cooling rate. As presented in Figure 15, the volume fraction ratio and number density ratio of Laves/NbC increase with the increase in cooling rate. It suggests that eutectic NbC compete to precipitate with Laves phase during liquid steel solidification, and increasing the cooling rate is more favorable to the precipitation of Laves phase.

The size of eutectic precipitates in 15Cr–22Ni–1Nb steel cannot be directly measured due to their irregular three-dimensional morphology. However, the average diameters of NbC and Laves phase can be calculated using Eq. [19][5] combined with the statistical results of volume fraction and number density.
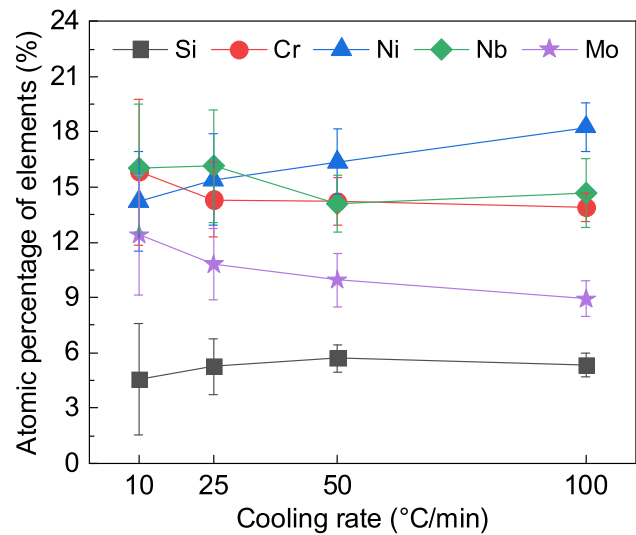
$$f = \left(\frac{1.4\pi}{6}\right) \cdot \left(\frac{ND^2}{S}\right) \qquad [19]$$

where f is the volume fraction of precipitates, S is the visual area (μm^2), N is the number of precipitates in the field of view, D is the average diameter of precipitates (μm).

The average size of eutectic NbC and Laves phase calculated with Eq. [19] is shown in Figure 16. The average size of Laves phase in the steel is greater than that of eutectic NbC at all cooling rates. Meanwhile, the average size of Laves phase decreases from 10.43 to 4.98 μm as the cooling rate is increased from 10 to 100 °C/min, and that of eutectic NbC decreases from 6.59 to 3.40 μm. On the one hand, the reduction in secondary dendrite arm spacing with increasing the cooling rate leads to a compression of the growth space of eutectic precipitates. On the other hand, the time for eutectic NbC and Laves phase growth is shortened as the cooling rate is increased.

The Laves phase in 15Cr–22Ni–1Nb steel is composed of ferrum, nickel, chromium, niobium, molybdenum and silicon. The content of alloying elements in the Laves phase is not only related to the chemical composition of the steel, but also influenced by the microsegregation degree of alloying elements and the competitive precipitation between eutectic NbC and Laves phase during liquid steel solidification. Due to the enhancement of microsegregation degree of alloying elements with increasing the cooling rate, the atomic percentage of silicon in the Laves phase increases from 4.55 to 5.71 pct with increasing the cooling rate from 10 to 50 °C/min, as presented in Figure 17. However, it decreases

Table V. Equilibrium Partition Coefficient k_γ and Diffusion Coefficient D_γ of Alloying Element in Austenitic Phase[28]

Alloying element	k_γ	$D_\gamma(\text{cm}^2/\text{s})$
C	0.34	$0.0761 \times \exp(-13\,4564/RT)$
Si	0.52	$0.3 \times \exp(-251470/RT)$
Ni	0.95	$0.34 \times \exp(-282391/RT)$
Cr	0.86	$0.0012 \times \exp(-219001/RT)$
Mo	0.585	$0.068 \times \exp(-246868/RT)$
Nb	0.22	$0.83 \times \exp(-266492/RT)$

slightly from 5.71 to 5.35 pct when the cooling rate is increased from 50 to 100 °C/min. It is because the number density of Laves phase in the steel increases significantly from 203.47 to 419.65 number/mm^2 as the cooling rate increases from 50 to 100 °C/min.

The atomic percentage of nickel in the Laves phase increases with the increase in cooling rate, whereas that of chromium decreases. It can be attributed to two factors. Firstly, the content of nickel forming Laves phase in the residual liquid steel is more abundant than that of chromium during liquid steel solidification. It is because nickel content (22.0 mass pct) in 15Cr–22Ni–1Nb steel is higher than chromium (15.5 mass pct), and the microsegregation degree of these two elements is basically the same in the steel.[2] Secondly, the number density of Laves phase increases quickly with increasing the cooling rate, which needs to consume more nickel and chromium.

The atomic percentage of niobium in the Laves phase increases slightly from 16.04 to 16.14 pct as the cooling rate is increased from 10 to 25 °C/min. However, it decreases from 16.14 to 14.09 pct with increasing the cooling rate from 25 to 50 °C/min. It is because NbC and Laves phase in the steel compete to precipitate during liquid steel solidification, and their number density increase quickly with the increase in cooling rate. When the cooling rate is increased from 50 to 100 °C/min, the atomic percentage of niobium slightly increases from 14.09 to 14.67 pct. It is because increasing the cooling rate is more favorable to the precipitation of Laves phase in comparison with NbC. As presented in Figure 15, the number density ratio of Laves/NbC in the steel increases from 1.14 to 1.38 as the cooling rate is increased from 50 to 100 °C/min. In addition, the atomic percentage of molybdenum decreases with increasing the cooling rate, which is due to the increase in the number density of Laves phase.

2. Microsegregation of alloying element

In the current study, the microsegregation degree of alloying element is characterized by the microsegregation ratio (C_L/C_0) calculated using the Lever-rule, Scheil–Gulliver and Clyne–Kurz models. The Lever-rule model assumes that the alloying element diffuses sufficiently to equilibrium in both the liquid and the solid during liquid steel solidification, as shown in Eq. [20][27]

$$C_L = C_0\left[1 - (1 - k_\gamma)x\right]^{-1} \qquad [20]$$

where C_L is the concentration of solute element in the residual liquid (mass pct), C_0 is the initial concentration of solute element (mass pct), k_γ is the equilibrium partition coefficient of solute element between austenite and liquid phase. Since the diffusion of alloying element in the solid is limited, especially for larger alloying element such as niobium and molybdenum, the Lever-rule model underestimates the concentration of alloying element in the residual liquid steel.

The Scheil–Gulliver model assumes that the alloying element does not diffuse in the solid, but completely diffuse in the liquid, as shown in Eq. [21].[27]

$$C_L = C_0[1 - x]^{k_\gamma - 1} \qquad [21]$$

The Scheil–Gulliver model overestimates the concentration of alloying element in the residual liquid steel, especially for smaller alloying element such as carbon.

In the present study, the Clyne–Kurz model is adopted to calculate the microsegregation ratio of alloying element to estimate the concentration of alloying element in the residual liquid steel at different cooling rates, as expressed in Eq. [22].[27]

$$C_L = C_0\left[1 - (1 - 2\Omega k_\gamma)x\right]^{\frac{(k_\gamma - 1)}{(1 - 2\Omega k_\gamma)}} \qquad [22]$$

$$\Omega = \alpha\left[1 - \exp\left(-\frac{1}{\alpha}\right)\right] - \frac{1}{2}\exp\left(-\frac{1}{2\alpha}\right) \qquad [23]$$

$$\alpha = \frac{D_\gamma t_f}{(0.5\lambda_2)^2} \qquad [24]$$

where D_γ is the diffusion coefficient of solute element in austenite phase. The Clyne-Kurz model takes the back diffusion of alloying element during liquid steel solidification into account. The equilibrium partition coefficient and diffusion coefficient of alloying elements are listed in Table V.
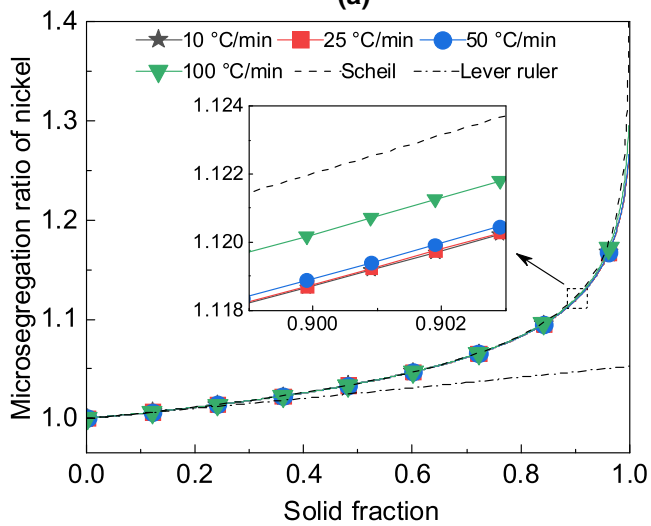
The microsegregation ratios of alloying elements calculated by the Lever-rule, Scheil–Gulliver and Clyne–Kurz model are shown in Figure 18. The equilibrium partition coefficients of carbon, silicon, nickel, chromium, niobium and molybdenum are smaller than 1. Therefore, these alloying elements are continuously enriched into the residual liquid steel, leading to the increase in their microsegregation ratios with increasing the solid fraction, especially at the terminal stage of solidification. The increase in the cooling rate enhances the microsegregation degree of alloying elements, especially niobium, molybdenum and silicon. The cooling rate exerts a negligible effect on the microsegregation ratios of carbon, nickel and chromium, as shown in Figure 18(a), (c) and (d). It is because the diffusion coefficient of carbon in austenite is large, and the equilibrium partition coefficient of nickel and chromium is close to one, as shown in Table V. Furthermore, the microsegregation ratio of carbon, silicon, nickel, chromium, niobium and molybdenum increases with the
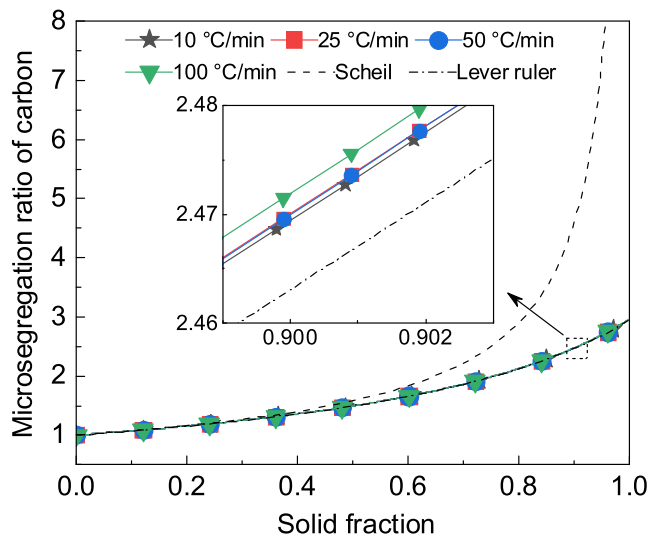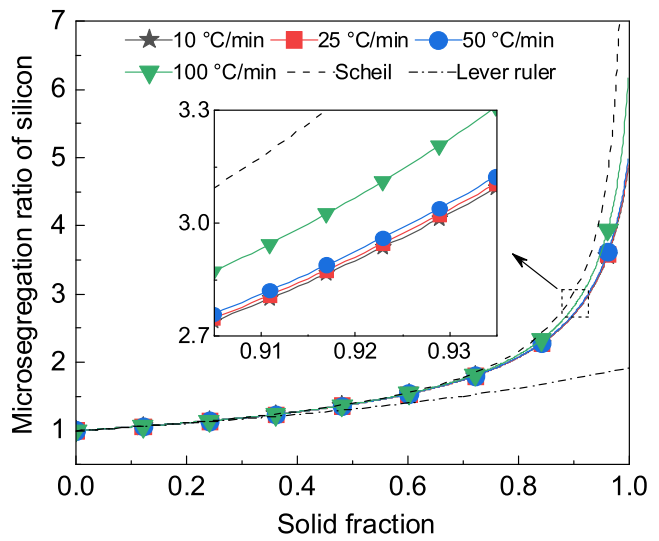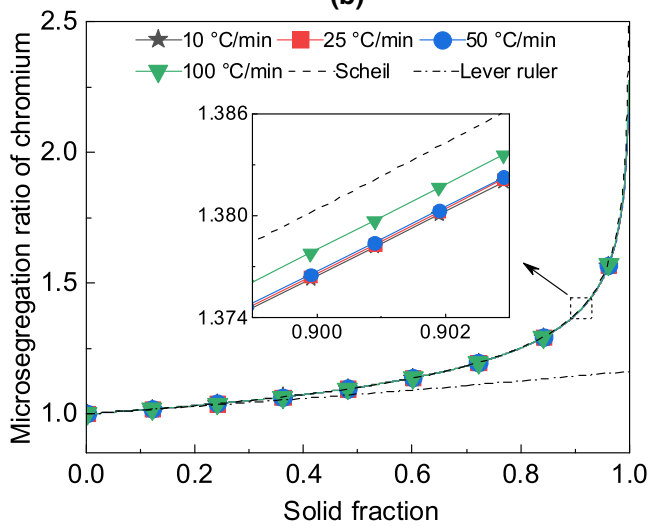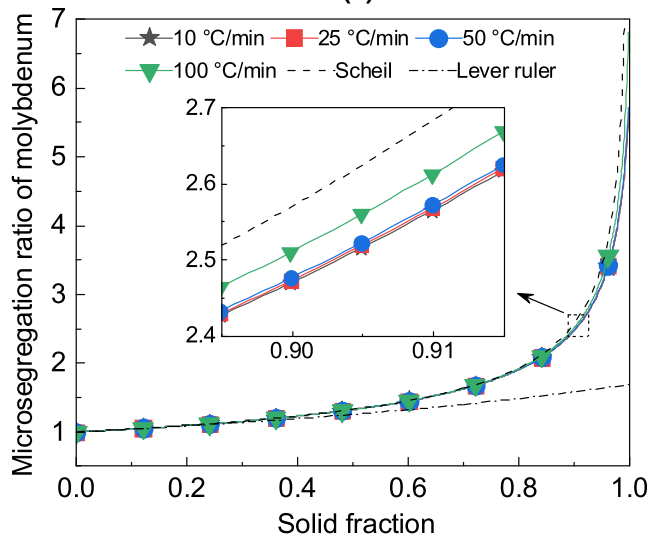
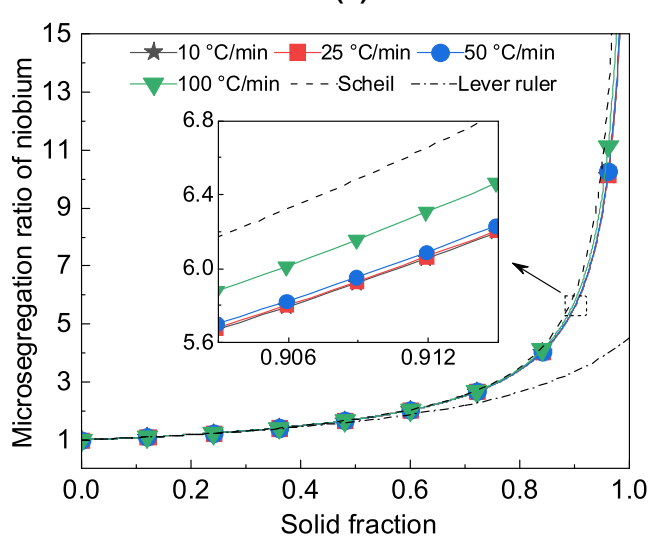Fig. 18—Variation of the microsegregation ratio of alloying element with solid fraction at different cooling rates. (*a*) carbon, (*b*) silicon, (*c*) nickel, (*d*) chromium, (*e*) molybdenum, (*f*) niobium.
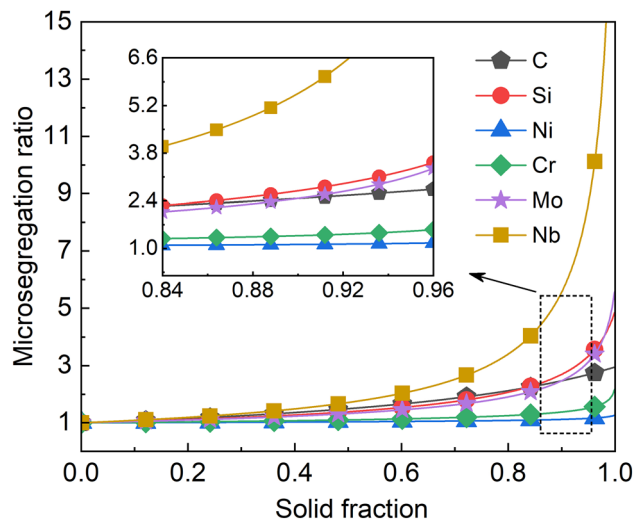
Fig. 19—Variation of microsegregation ratios of alloying elements with solid fraction at the cooling rate of 10 °C/min.
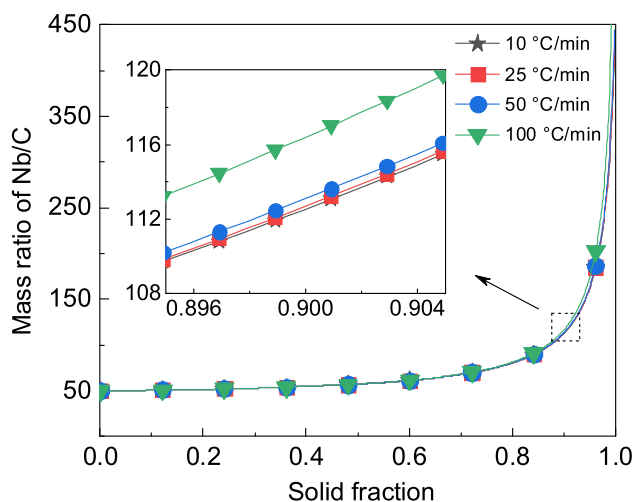

Fig. 20—Variation of the mass ratio of Nb/C in the residual liquid steel with solid fraction at different cooling rates.

increase in cooling rate. However, the increment of microsegregation ratio with cooling rate is quite small. It is because the volume fraction of eutectic precipitates in 15Cr–22Ni–1Nb steel is very small (< 0.8 pct, as illustrated in Figure 13).

The microsegregation ratio of silicon, nickel, chromium, niobium and molybdenum calculated by the Clyne–Kurz model is close to the value calculated by the Scheil–Gulliver model, indicating that the back diffusion of these elements in the solid phase is restricted during liquid steel solidification. Meanwhile, this restrictive effect on the back diffusion becomes stronger at a higher cooling rate, which leads to more alloying elements accumulated in the residual liquid steel. The microsegregation ratio of carbon calculated by the Clyne–Kurz model is closed to that calculated by the Lever-rule model, and thus carbon atoms diffuse nearly to

equilibrium between the residual liquid steel and the austenite phase during solidification. It is attributed to a large diffusion coefficient of carbon in austenite.

Figure 19 compares the microsegregation ratio of different alloying elements at the cooling rate of 10 °C/min. When the solid fraction is 0.9, the microsegregation ratios of niobium, silicon, molybdenum, carbon, chromium and nickel are 5.59, 2.70, 2.48, 2.47, 1.38 and 1.12, respectively. The microsegregation degree of niobium in 15Cr–22Ni–1Nb steel is the largest, followed by silicon, molybdenum and carbon at the same level. The microsegregation of chromium and nickel basically do not occur because their microsegregation ratios are close to one. The microsegregation degree of alloying element is in connection with its equilibrium partition coefficient and diffusion coefficient. The order of microsegregation ratio of alloying element is niobium > silicon > molybdenum > chromium > nickel because the equilibrium partition coefficient is in the order of niobium < silicon < molybdenum < chromium < nickel < 1, as listed in Table V. It is noted that the equilibrium partition coefficient of carbon between austenite and liquid phase is small, but its diffusion coefficient in the austenite is very large. Hence, the microsegregation degree of carbon in the steel is at the same level as that of silicon and molybdenum.

The higher Nb/C ratio in steel is generally favorable to the formation of Laves phase.[1] The Clyne-Kurz model was used to calculate the mass ratio of Nb/C in the residual liquid steel to clarify the mechanism of the change in the volume fraction ratio and number density ratio of Laves/NbC with the cooling rate. As shown in Figure 20, the mass ratio of Nb/C becomes higher as the solid fraction increases, especially in the terminal stage of solidification. More Laves phases will precipitate in the steel compared with eutectic NbC as the solidification proceeds. When the solid fraction reaches to 0.9, the mass ratio of Nb/C is 113.07, 113.22, 113.63 and 117.01 at the cooling rates of 10, 25, 50 and 100 °C/min, respectively. Consequently, increasing the cooling rate exerts a positive impact on promoting the increase in the volume fraction ratio and number density ratio of Laves/NbC in the steel.

3. Thermodynamic consideration on eutectic precipitate formation

The precipitation of eutectic precipitates in 15Cr–22Ni–1Nb steel start directly from the solute-rich residual liquid steel in the terminal period of solidification when the critical thermodynamic conditions are reached. The Gibbs free energy change (ΔG) for the reaction of eutectic precipitate formation during liquid steel solidification is calculated to reveal the influence of cooling rate on their precipitation behaviors.

The authors' previous study[1] demonstrated the Laves phase in 15Cr–22Ni–1Nb steel can be simplified to Fe_2Nb for thermodynamic consideration. The standard Gibbs free energy change ΔG^o for the reactions of eutectic NbC and Fe_2Nb formation is calculated (the parameters are shown in Table VI), as presented in Table VII. f_{Nb} and f_C shown in Table VII are the activity

coefficient of niobium and carbon in the liquid steel, respectively, and can be obtained by the following formula[15]:

$$\lg f_i = e_i^i[\text{pct } i] + \sum e_i^j[\text{pct } j] \quad [25]$$

where e_i^j is the activity interaction coefficient of element j to i, which is cited from Reference 29. [pct i] is the mass percentage of element i in the residual liquid steel, which is calculated by the Clyne-Kurz model.

The variation of the Gibbs free energy change for the reaction of eutectic NbC and Laves phase formation with solid fraction is presented in Figure 21. The values of Gibbs free energy change for the chemical reactions of eutectic NbC and Laves phase formation decrease as the solid fraction increases. The starting-precipitation solid fraction of eutectic precipitates in the steel at

different cooling rates are obtained according to Figure 21, as shown in Figure 22. The solid fraction corresponding to the starting-precipitation of eutectic NbC increases from 0.892 to 0.903 as the cooling rate is increased from 10 to 25 °C/min, and the starting-precipitation solid fraction of Laves phase increases from 0.916 to 0.922. Nevertheless, the solid fraction at which eutectic NbC starts to precipitate decreases from 0.903 to 0.829, and the starting-precipitation solid fraction of Laves phase is lowered from 0.922 to 0.879 when the cooling rate is increased from 25 to 100 °C/min.

Increasing the cooling rate generally promotes the precipitation of eutectic precipitates during liquid steel solidification. However, in the current study, the solid fraction corresponding to the starting-precipitation of eutectic precipitates in the steel increases first, and then decreases with the increase in cooling rate. The influence of cooling rate on initiation and finishing solidification temperature plays a decisive role on the starting-precipitation solid fraction of eutectic precipitates in the steel. It is because the variation of starting-precipitation solid fraction of eutectic NbC and Laves phase with the cooling rate is consistent with the change in the initiation and finishing solidification temperature with the cooling rate, as presented in Figure 22.

Table VI. Standard Gibbs Free Energy Change for Chemical Reaction

Chemical Reaction	$\Delta G°$(J/mol)	References
$\text{Fe}_{(s)} = [\text{Fe}]$	$13807 - 7.61T$	[30]
$\text{C}_{(s)} = [\text{C}]$	$22594 - 42.26T$	[31]
$\text{Nb}_{(s)} = [\text{Nb}]$	$23012 - 52.30T$	[31]
$\text{Nb}_{(s)} + \text{C}_{(s)} = \text{NbC}_{(s)}$	$-136901 + 2.43T$	[30]
$2\text{Fe}_{(s)} + \text{Nb}_{(s)} = \text{Fe}_2\text{Nb}_{(s)}$	$-54600 + 11.40T$	[32]

Table VII. Gibbs Free Energy Change for the Reaction of Eutectic NbC and Fe$_2$Nb Formation

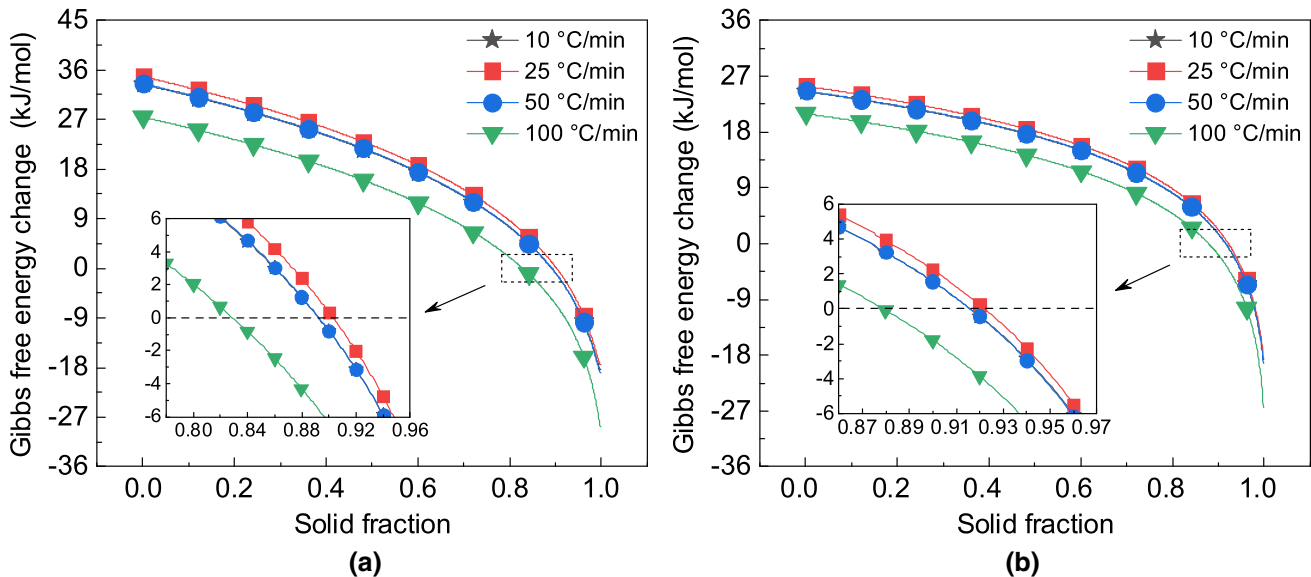| Reaction	$\Delta G°$ (J/mol)	ΔG (J/mol)
$[\text{Nb}] + [\text{C}] = \text{NbC}_{(s)}$	$-182507 + 96.99T$	$\Delta G°_{\text{NbC}} + RT\ln\frac{1}{f_{\text{Nb}}[\text{pct Nb}] \cdot f_C[\text{pct C}]}$
$2[\text{Fe}] + [\text{Nb}] = \text{Fe}_2\text{Nb}_{(s)}$	$-105226 + 78.92T$	$\Delta G°_{\text{Fe}_2\text{Nb}} + RT\ln\frac{1}{f_{\text{Nb}}[\text{pct Nb}] \times 1}$

Fig. 21—Variation of Gibbs free energy change for the chemical reaction of eutectic precipitate formation with solid fraction at different cooling rates. (*a*) NbC, (*b*) Laves phase.
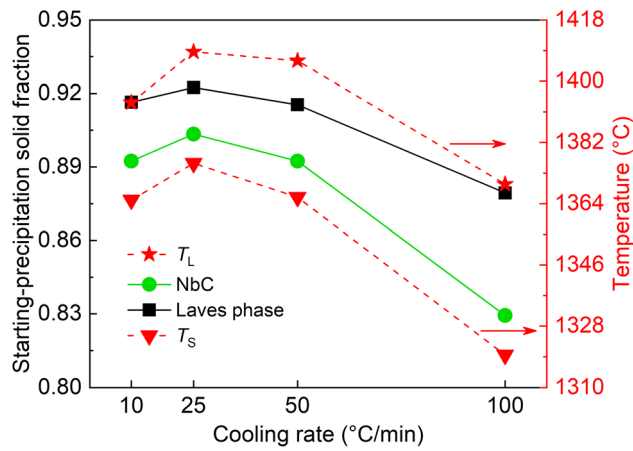
Fig. 22—Relationship between the starting-precipitation solid fraction of eutectic precipitates and cooling rates.

Fig. 23—Relationship between the starting-precipitation temperature of eutectic precipitates and cooling rates.

The starting-precipitation temperature of eutectic precipitates at different cooling rates can be calculated by taking the value of starting-precipitation solid fraction into Eq. [6]. As presented in Figure 23, the starting-precipitation temperature of eutectic NbC increases from 1641.7 K to 1651.8 K (1368.7 °C to 1378.8 °C) with increasing the cooling rate from 10 to 25 °C/min, whereas it decreases from 1651.8 K to 1600.7 K (1378.8 °C to 1327.7 °C) when the cooling rate is increased from 25 to 100 °C/min. Although the formation of eutectic NbC in the steel is prior to the Laves phase during liquid steel solidification, there is a negligible difference between their starting-precipitation temperatures. The starting-precipitation temperature of Laves phase increases from 1641.2 K to 1651.5 K (1368.2 °C to 1378.5 °C) as the cooling rate is increased from 10 to 25 °C/min, and it decreases from 1651.5 K to 1599.5 K (1378.5 °C to 1326.5 °C) with increasing the cooling rate from 25 to 100 °C/min. The change in the starting-precipitation temperature of eutectic NbC and Laves phase with the cooling rate can be ascribed to the variation of initiation and finishing solidification temperatures with the cooling rate.

To further illustrate the role of cooling rate on the precipitation behaviors of eutectic NbC and Laves phase during liquid steel solidification, the precipitation tendency of eutectic precipitate in steel is defined thermodynamically as Eq. [26].

$$\rho_t = -\frac{d\Delta G}{dx} \qquad [26]$$

It should to be noted that a larger value of ρ_t indicates that the precipitation tendency of eutectic precipitate is stronger. In the current study, the precipitation tendency of eutectic precipitates with the solid fraction between 0.8 and 1 is calculated since the starting-precipitation solid fraction of eutectic precipitates in the steel is greater than 0.8.

Figure 24 presents the change in the precipitation tendency of eutectic precipitates in the steel with solid fraction at different cooling rates. As shown in Figure 24(a), the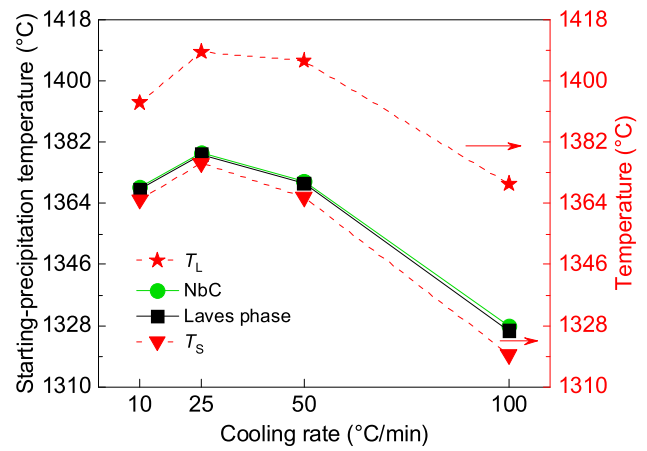 precipitation tendency of eutectic NbC increases first as the solid fraction increases, and then decreases markedly in the final period of solidification. It could be because a lower carbon content (0.02 mass pct) in the steel limits the precipitation of eutectic NbC. The critical solid fraction at which the precipitation tendency of eutectic NbC begins to decrease is 0.989, 0.990, 0.991 and 0.994 at the cooling rates of 10, 25, 50 and 100 °C/min, respectively. The precipitation tendency of Laves phase increases constantly as the solid fraction increases, as shown in Figure 21(b). Although the starting-precipitation solid fraction and starting-precipitation temperature of eutectic NbC and Laves phase increase first and then decrease as the cooling rate increases, their precipitation tendency keeps becoming stronger.

Figure 25 shows the change in the precipitation tendency ratio of Laves/NbC with solid fraction at the cooling rates of 10, 25, 50 and 100 °C/min. At a higher cooling rate, the eutectic NbC has a stronger precipitation tendency compared with that of Laves phase during liquid steel solidification. Furthermore, the ratio of the precipitation tendency of Laves phase to that of eutectic NbC increases as the solid fraction increases, which is because the mass ratio of Nb/C in the residual liquid steel becomes higher with increasing the solid fraction.

IV. CONCLUSIONS

(1) The initiation and finishing solidification temperatures of the steel increase first as the cooling rate is increased from 10 to 25 °C/min, and then decrease with further increasing the cooling rate from 25 to 100 °C/min. The solidification temperature interval of the steel is monotonically enlarged as the cooling rate is increased. A relationship between the final solidification time and cooling rate is established as $t_f = 35.04 \cdot v^{-0.83}$.

(2) The rate constant of austenitic nucleation and growth decreases with increasing the cooling rate from 10 to 100 °C/min due to the reduction in the
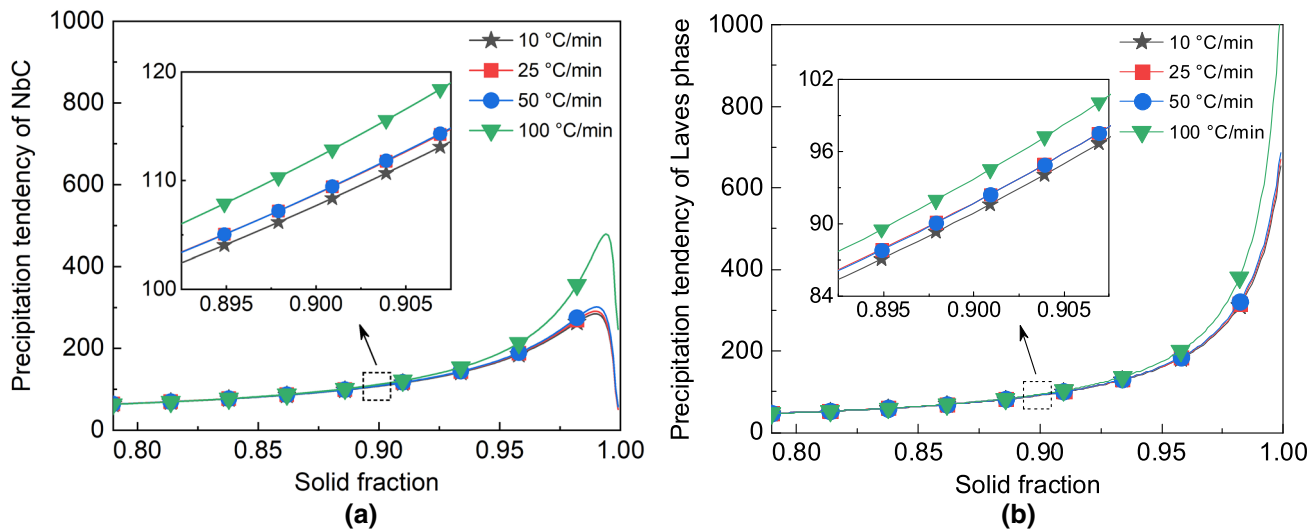
Fig. 24—Variation of the precipitation tendency of eutectic precipitates with solid fraction at different cooling rates. (*a*) NbC, (*b*) Laves phase.

effective activation energy of liquid steel solidification, leading to a decrease in the initiation solidification temperature of liquid steel. Nevertheless, a higher cooling rate results in a greater nucleation rate of austenite, and thus the initial nucleation is more likely to occur at higher temperatures. The effective activation energy of austenitic nucleation and growth is − 88.86 and − 396.76 kJ/mol, respectively.

(3) The secondary dendrite arm spacing of the solidified steel is reduced from 69.43 to 27.27 μm as the cooling rate is increased from 10 to 100 °C/min. The relationship between the secondary dendrite arm spacing, temperature gradient and solidification growth rate is expressed as $\lambda_2 = 165.56 \cdot (GV)^{-0.39}$.

(4) The morphological dimensions of eutectic NbC and Laves phase are continuously compressed with increasing the cooling rate. As the cooling rate is increased, the volume fraction and number density of eutectic NbC and Laves phase increase, as well as the volume fraction ratio and number density ratio of Laves/NbC. The atomic percentage of Laves phase-forming alloying element (Si, Ni, Cr, Nb and Mo) changes with the variation of cooling rate.

(5) Increasing the cooling rate inhibits the back diffusion of alloying element from liquid to solid, resulting in its larger microsegregation degree, especially for Nb, Si and Mo. The cooling rate has a negligible effect on the microsegregation degree of C, Cr and Ni. The microsegregation degree of Nb is the largest irrespective of the cooling rate, followed by Si, Mo and C. The mass ratio of Nb/C in the residual liquid steel increases as the cooling rate is increased, which enhances the precipitation of Laves phase.

(6) The starting-precipitation solid fraction and starting-precipitation temperature of eutectic NbC and Laves phase increase first as the cooling rate is in-
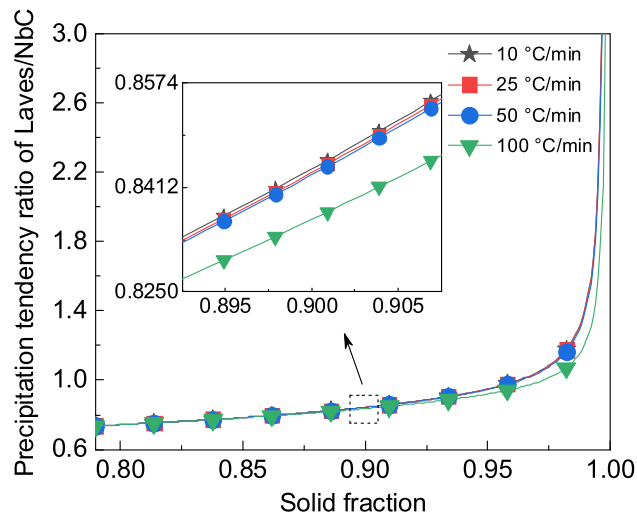

Fig. 25—Change in the precipitation tendency ratio of Laves/NbC with solid fraction at different cooling rates.

creased from 10 to 25 °C/min, and then decrease with increasing the cooling rate from 25 to 100 °C/min. The precipitation of eutectic NbC is prior to the Laves phase during the solidification of the steel. The precipitation tendencies of eutectic NbC and Laves phase increase as the cooling rate is increased.

CONFLICT OF INTEREST

On behalf of all authors, the corresponding author states that there is no conflict of interest.

REFERENCES

1. H.C. Xu, C.B. Shi, X. Zhu, S.J. Wang, J. Li, and S.Z. Wang: *J. Iron Steel Res. Int.*, 2022, vol. 29, pp. 1823–35.
2. X. Zhu, C.B. Shi, S.J. Wang, P. Lan, and J. Li: *J. Iron Steel Res. Int.*, 2023, vol. 30, pp. 338–49.
3. C.B. Shi, H.C. Xu, S.J. Wang, J. Li, and X. Zheng: *Mater. Charact.*, 2021, vol. 182, p. 111564.
4. X. Zheng, C.B. Shi, X. Zhu, and H.C. Xu: *Metall. Mater. Trans. B*, 2022, vol. 53B, pp. 877–94.
5. C.B. Shi, X. Zhu, X. Zheng, P. Lan, and J. Li: *Mater. Sci. Eng. A*, 2022, vol. 854, p. 143822.
6. C.B. Shi, Q.T. Zhu, W.T. Yu, H.D. Song, and J. Li: *J. Mater. Eng. Perform.*, 2016, vol. 25, pp. 4785–95.
7. Y.P. Zhang, D.P. Zhan, X.W. Qi, and Z.H. Jiang: *J. Mater. Sci. Technol.*, 2019, vol. 35, pp. 1240–49.
8. F. Ji, R. Xu, Y.L. Gao, Q.C. Tian, L. Wang, Z.X. Xiao, and F.X. Yin: *J. Iron Steel Res. Int.*, 2021, vol. 28, pp. 1591–1604.
9. X. Shi, S.C. Duan, W.S. Yang, H.J. Guo, and J. Guo: *Metall. Mater. Trans. B*, 2018, vol. 49B, pp. 1883–97.
10. M. Bleckmann, J. Gleinig, J. Hufenbach, H. Wendrock, L. Giebeler, J. Zeisig, U. Diekmann, J. Eckert, and U. Kühn: *J. Alloys Compd.*, 2015, vol. 634, pp. 200–07.
11. Q. Wang, L.J. Wang, W. Zhang, and K. Chou: *Metals*, 2023, vol. 13, p. 246.
12. X.F. Zhou, F. Fang, F. Li, and J.Q. Jiang: *J. Mater. Sci.*, 2011, vol. 46, pp. 1196–1202.
13. J.C. Liu, W.M. Li, and L. Fu: *Steel Res. Int.*, 2022, vol. 93, p. 2200137.
14. Y.S. Hao, J. Li, X. Li, W.C. Liu, G.M. Cao, C.G. Li, and Z.Y. Liu: *J. Mater. Process. Technol.*, 2020, vol. 275, p. 116326.
15. B.J. Kooi: *Phys. Rev. B*, 2004, vol. 70, p. 224108.
16. H.R. Wang, Y.L. Gao, Y.F. Ye, G.H. Min, Y. Chen, and X.Y. Teng: *J. Alloys Compd.*, 2003, vol. 353, pp. 200–06.
17. A.A. Soliman, S. Al-Heniti, A. Al-Hajry, M. Al-Assiri, and G. Al-Barakati: *Thermochim. Acta*, 2004, vol. 413, pp. 57–62.
18. M. Vasić, D.M. Minić, V.A. Blagojević, and D.M. Minić: *Thermochim. Acta*, 2013, vol. 572, pp. 45–50.
19. C.B. Shi, M.D. Seo, H. Wang, J.W. Cho, and S.H. Kim: *Metall. Mater. Trans. B*, 2015, vol. 46B, pp. 345–56.
20. T. Hart-Rawung, J. Buhl, A. Horn, M. Bambach, and M. Merklein: *J. Mater. Process. Technol.*, 2023, vol. 313, p. 117856.
21. G. Ruitenberg, E. Woldt, and A.K. Petford-Long: *Thermochim. Acta*, 2001, vol. 378, pp. 97–105.
22. Q. Wang, L.J. Wang, W. Zhang, J.M. Li, and K.C. Chou: *Metall. Mater. Trans. B*, 2020, vol. 51B, pp. 1773–83.
23. J.W. Christian: *The Theory of Transformations in Metals and Alloys*, Pergamon Press, Oxford, 2002, pp. 545–46.
24. F. Liu, F. Sommer, C. Bos, and E.J. Mittemeijer: *Int. Mater. Rev.*, 2007, vol. 52, pp. 193–212.
25. P.R. Sahm, H. Jones, and C. Adam: *Science and Technology of the Undercooled Melt: Rapid Solidification Materials and Technologies*, Springer, Netherlands, 2012, pp. 29–51.
26. M.T. Mao, H.J. Guo, F. Wang, and X.L. Sun: *ISIJ Int.*, 2019, vol. 59, pp. 848–57.
27. Y.M. Won and B.G. Thomas: *Metall. Mater. Trans. A*, 2001, vol. 32A, pp. 1755–67.
28. Y.A. Meng and B.G. Thomas: *Metall. Mater. Trans. B*, 2003, vol. 34B, pp. 685–706.
29. T. Matsushita and K. Mukai: *Chemical Thermodynamics in Materials Science: From Basics to Practical Applications*, Springer, Singapore, 2018, pp. 246–51.
30. E.T. Turkdogan: *Physical Chemistry of High Temperature Technology*, Academic Press, New York, 1980, pp. 7–11.
31. G.K. Sigworth and J.F. Elliott: *Met. Sci.*, 1974, vol. 8, pp. 298–310.
32. J.H. Zhu, C.T. Liu, L.M. Pike, and P.K. Liaw: *Intermetallics*, 2002, vol. 10, pp. 579–95.